Supplementary Information

Synergistic dual-functional layer-modified Cu current collector by Co-FCVA apparatus for high-performance anode-free lithium metal batteries

Yaohui Zhu[1], Shengqi Dai[1], Shengjie Du[1], Bo Zhang[1], Lin Chen[2,*],and Bin Liao[1,2,*]

[1] Key Laboratory of Beam Technology of the Ministry of Education, School of Physics and Astronomy, Beijing Normal University, Beijing 100875, China
[2] Laboratory of Beam Technology and Energy Materials, Advanced Institute of Natural Sciences, Beijing Normal University, Zhuhai 519087, China.

Correspondence
Prof. Bin Liao
Key Laboratory of Beam Technology of the Ministry of Education, School of Physics and Astronomy, Beijing Normal University, 100875 Beijing, China
E-mail: liaobingz@bnu.edu.cn
Dr. Lin Chen
Laboratory of Beam Technology and Energy Materials, Advanced Institute of Natural Sciences, Beijing Normal University, Zhuhai 519087, China.
E-mail: 91122023020@bnu.edu.cn

A new type of Co-FCVA device was used to modify the Cu current collector. The schematic diagram of the Co-FCVA system is shown in **Figure S1**, which consists of two or more cathode sources. The target material of the cathode is ionized using a metal vapor vacuum arc (MEVVA) source, and the generated metal ions are filtered through a magnetic field to remove some neutral particles or large droplets. This process ensures that the thin film deposited on the substrate is homogenized. In addition, by introducing a pulse negative bias voltage on the sample placement plate, the stability of the adhesion between the deposited thin film and the substrate (current collector) is ensured.

1. Experimental Section

Preprocessing process: First, we chose the commercial 9 μm thick copper foil used as the current collector, and then the copper foil was pre-cut to a size of 100mm×100mm. Subsequently, the copper foil sample was placed in ultrasonic cleaning equipment for acid washing, using 0.1 M hydrochloric acid for 2 hours. Subsequently, the cleaned samples were soaked and cleaned in acetone solution and ethanol solution for 5 minutes. The soaked copper foil samples were rinsed with deionized water and then placed in a vacuum drying oven for drying for 2 hours. Select high-purity metal targets as cathode sources (Al and Zn targets, size: Φ 100 mm × 20 mm, purity 99.90%).

Preparation of Zn-AlN@Cu: Initially, the preprocessed copper foil was positioned on the sample stage, and subsequently, the vacuum level in the vacuum chamber was elevated to 3×10^{-3} Pa. The cathode source was then excited with an arc current 80A to ionize the metal target. The filter current was set at 2A, accompanied by the introduction of a 100V pulse negative bias voltage with a duty cycle of 80%. Following this, the sample was aligned with the deposition port corresponding to the Zn target, the control power was activated, and the Zn layer was deposited at a rate of 35 nm per minute. After 345 seconds of deposition, a Zn layer with a thickness of approximately 200 nm was achieved. Subsequently, the power was disengaged, and the sample stage was repositioned to the deposition port corresponding to the Al target. At this juncture, the valve was opened, and N_2 was introduced into the

chamber at a flow rate of 50 sccm, attaining a vacuum level of 4.5×10^{-2} Pa. The control power was then initiated, and the AlN layer was deposited at a rate of approximately 40 nm per minute. After 150 seconds of deposition, an AlN layer of about 100nm thickness was obtained.

Preparation of Zn@Cu and AlN@Cu: Similar to the preparation method for Zn-AlN@Cu, a single deposition port is employed for the deposition of either the Zn layer or the AlN layer.

Characterization: To obtain the morphological characteristics of the material, the surface and cross-sectional morphology of CCs were observed using a cold field emission scanning electron microscope (SEM, S-4800, Hitachi, Tokyo, Japan) for material preparation characterization. The sample surface components were characterized by X-ray photoelectron spectroscopy (XPS, Thermo Scientific K-Alpha, USA, using an Al Kα (1486 eV) anode). Atomic force microscopy (AFM, Tosca 400, Anton Paar) in tapping mode is used to observe the surface topography of the sample. The surface crystallographic characteristics of the samples were characterized using an X-ray diffractometer (XRD, Rigaku SmartLab SE, Japan).

Electrochemical testing: All samples were assembled into standard CR2032 coin-type batteries and filled with argon gas at room temperature in a glove box with water and oxygen content below 0.1 ppm. Cell testing was conducted using a multi-channel cell tester (LAND, CT-2001A) at a constant temperature of 25°C. Using the commercially available dry unidirectional stretching process polypropylene (UOPP) separator (with a diameter of 16 mm), CCs are cut into small circles with a diameter of 10mm using cutting equipment. All anode CCs (modified and unmodified) and separators are first dried in a vacuum drying chamber for 2 hours before assembling the battery. Each battery uses 60 μL and 10 μL (lean electrolyte) electrolyte (1 M LiTFSI in 1, 3-dioxane (DOL)/1, 2-dimethoxymethyl methane (DME) (v/v=1:1), 1 wt% $LiNO_3$). The half-cell test uses lithium foil as the counter electrode, while the symmetrical cell test uses CC pre-deposited lithium as the electrode. The subsequent full cell testing used $LiFePO_4$ (LFP) as the cathode and CCs (modified and unmodified) as the anode. The preparation of cathode LFP was carried out using methyl pyrrolidone (NMP) as a

solvent. Commercial LFP powder, acetylene black, and PVDF were uniformly mixed in a mass ratio of 8:1:1 to form a slurry. Then, evenly apply the slurry onto the commercial carbon-coated aluminum foil with a scraper, and place it in a blower driver drying room at 60 °C for 2 hours to remove most of the solvent on the surface. Subsequently, transfer the sample to a vacuum drying chamber and maintain it at 60 °C for 10 hours to eliminate any residual solvents. Finally, use cutting equipment to cut the cathode into circular pieces with a diameter of 10 mm. Electrochemical impedance spectroscopy (EIS) was performed on the battery using an electrochemical workstation (PARSTAT 2273, China) in the frequency range of 100 kHz to 0.01 Hz, and CV curves were collected under different scanning rate conditions.

2. Density Functional Theory (DFT) calculations

In order to investigate the interactions between lithium ions and various material surfaces, we constructed an adsorption model to calculate the adsorption energy between lithium ions and various interfaces. Initially, we established seven slab models, specifically Cu (100), Cu (110), Cu (111), Zn (100), Zn (002), AlN (100), and AlN (002). All seven models were constructed from 3×3 unit cells, and each model exhibited a four-layer repeated periodic structure along the Z-axis, with an additional 15 Å vacuum layer above the periodic structure. Subsequently, the top two layers of the four-layer structure were designated as relaxed atomic layers, while the bottom two layers were set as fixed atomic layers. All Density Functional Theory (DFT) calculations were performed using the Vienna Ab initio Simulation Package (VASP). The exchange-correlation interactions were described using the Perdew-Burke-Ernzerhof (PBE) form of the Generalized -Gradient Approximation (GGA). Additionally, the cutoff energy for Cu was set to 400 eV, and for Zn and AlN, it was set to 500 eV. Self-consistent-field (SCF) calculations were conducted until both the total energy difference between the two iterations and the forces on atoms converged to within 1×10^{-6} eV and less than 0.02 eV/Å, respectively. For Brillouin zone sampling, Cu employed Monkhorst−Pack k-points of $6 \times 6 \times 2$, Zn utilized Monkhorst−Pack k-points of $6 \times 6 \times 1$, and AlN used Monkhorst−Pack k-points of $3 \times 3 \times 1$.

The adsorption energy between lithium ion and adsorbent substrate surface can be calculated as follows:

$$E_{ads} = E_{Li+sur} - E_{sur} + E_{Li}$$

Here, E_{Li+sur} denotes the energy of the complete adsorption system, E_{sur} represents the energy of the adsorbent substrate surface, and E_{Li} signifies the energy of a single lithium atom/ion. A more negative E_{ads} value signifies an enhanced adsorption capability of the adsorbate atom/ion on the adsorbent surface, indicating a heightened inclination for stable adsorption on the surface.
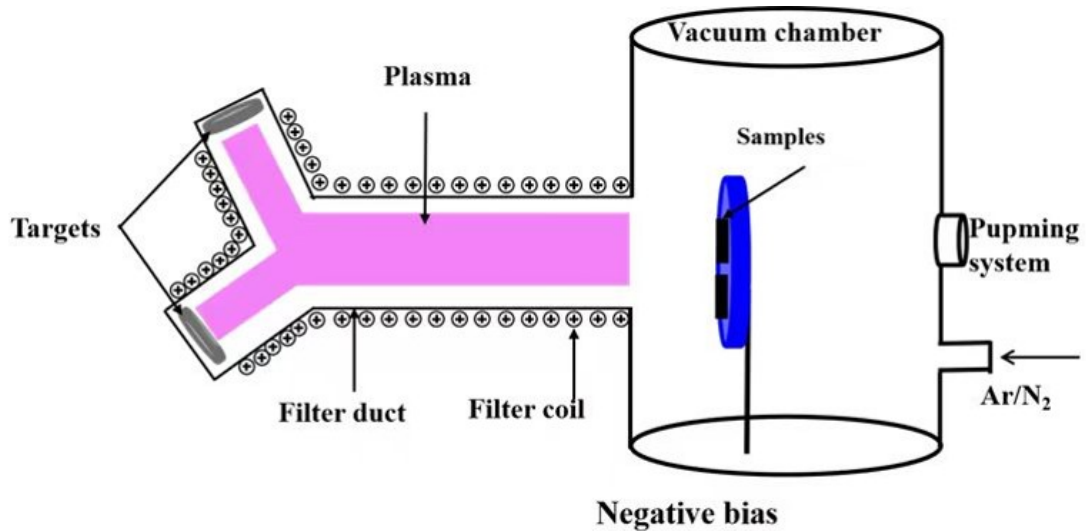

**Figure S1.** Overview diagram of Co-FCVA equipment principle
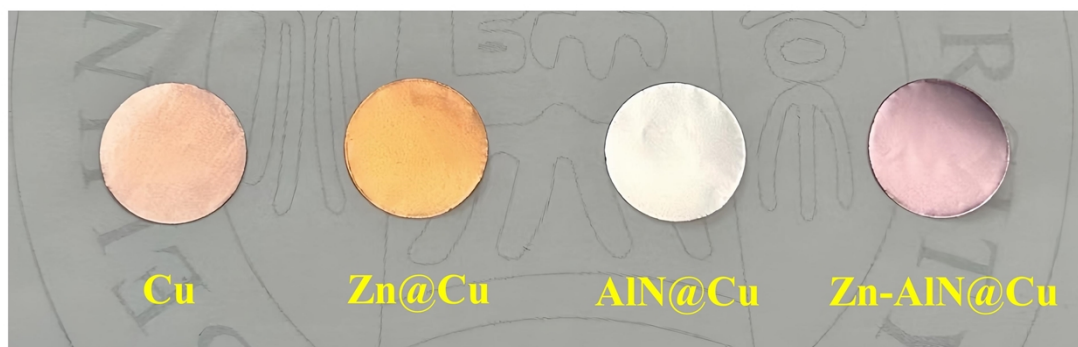
**Figure S2.** Photographs of the bare Cu, Zn@Cu, AlN@Cu, and Zn-AlN@Cu.
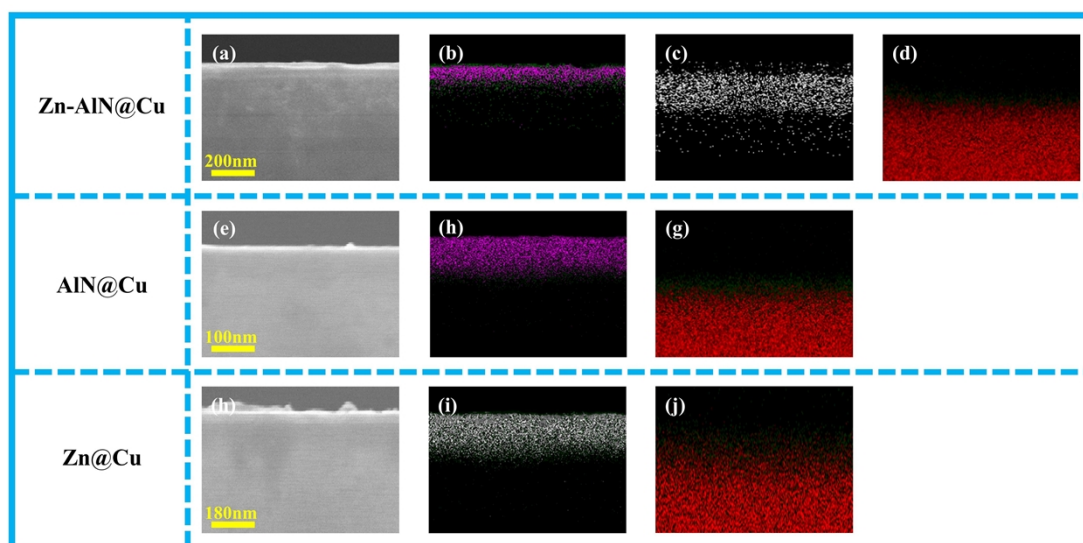
Figure S3. Distribution of cross-sectional elements in different samples. (a) SEM image of the cross-section of the Zn-AlN layer. EDS mapping images of (b) Al, (c) Zn, and (d) Si. (e) SEM image of the cross-section of the AlN layer. EDS mapping images of (f) Al and (g) Substrate. (h) SEM image of the cross-section of the Zn layer. EDS mapping image of (i) Zn and (j) Cu on the substrate.
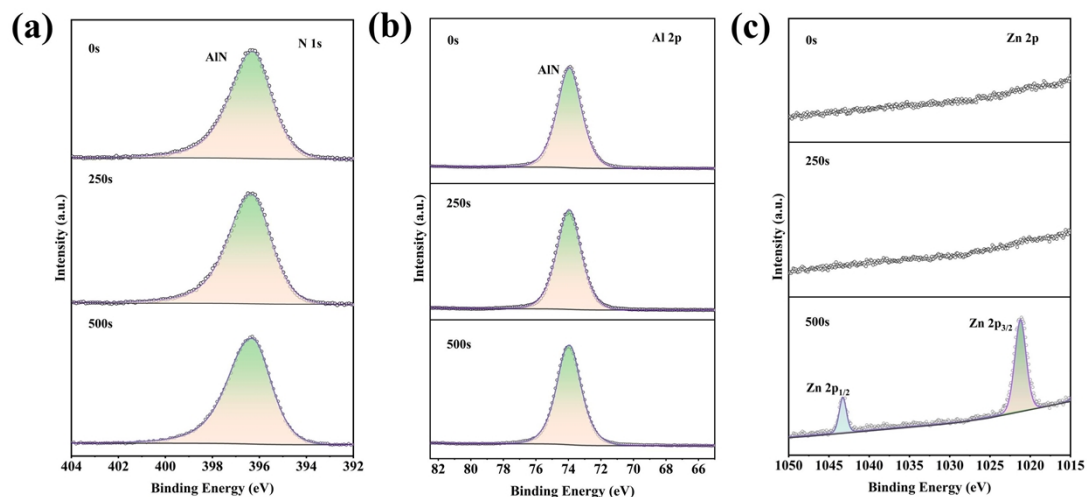
Figure S4. In-depth XPS spectra of AlN@Cu CC, (a) N 1s, (b) Al 2p, and (c) Zn 2p.
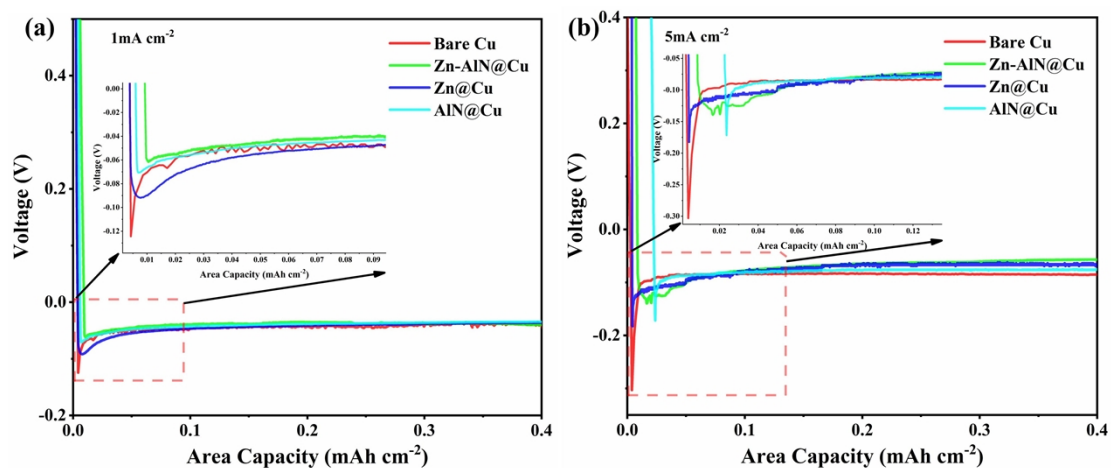

Figure S5. (a) voltage-area capacity curves of Li nucleation on the bare Cu, Zn-AlN@Cu, Zn@Cu, and AlN@Cu at a current density of 1 mA cm^{-2}. (b) voltage-area capacity curves of Li nucleation on the bare Cu, Zn-AlN@Cu, Zn@Cu, and AlN@Cu at a current density of 5 mA cm^{-2}.
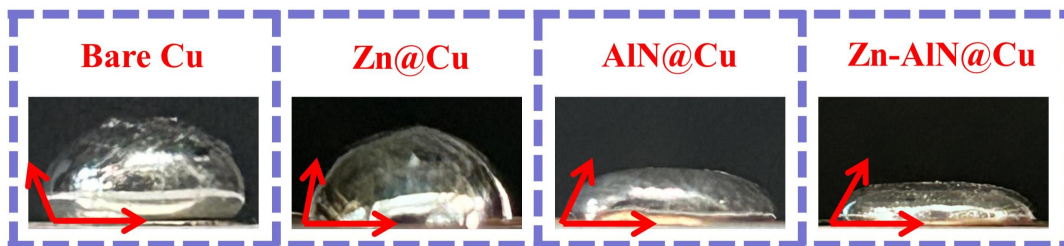
Figure S6. Wettability of molten lithium at 240° C on different current collector surfaces, contact angle optical images of bare Cu, Zn@Cu, AlN@Cu, and Zn-AlN@Cu.
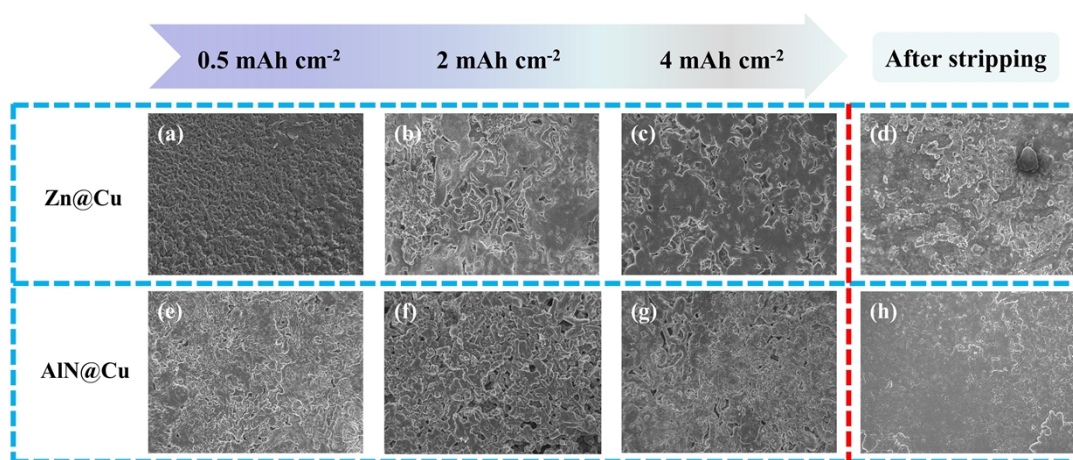

Figure S7. SEM images of Zn@Cu CCs after plating quantitative Li capacities of (a) 0.5 mAh cm $^{-2}$, (b) 2 mAh cm $^{-2}$, (c) 4 mAh cm $^{-2}$, and (d) after stripping. SEM images of AlN@Cu CCs after plating quantitative Li areal capacities of (e) 0.5 mAh cm $^{-2}$, (f) 2 mAh cm $^{-2}$, (g) 4 mAh cm $^{-2}$, and (h) after stripping.
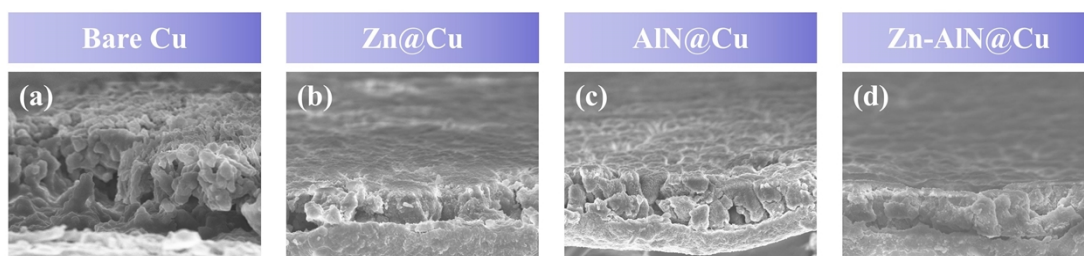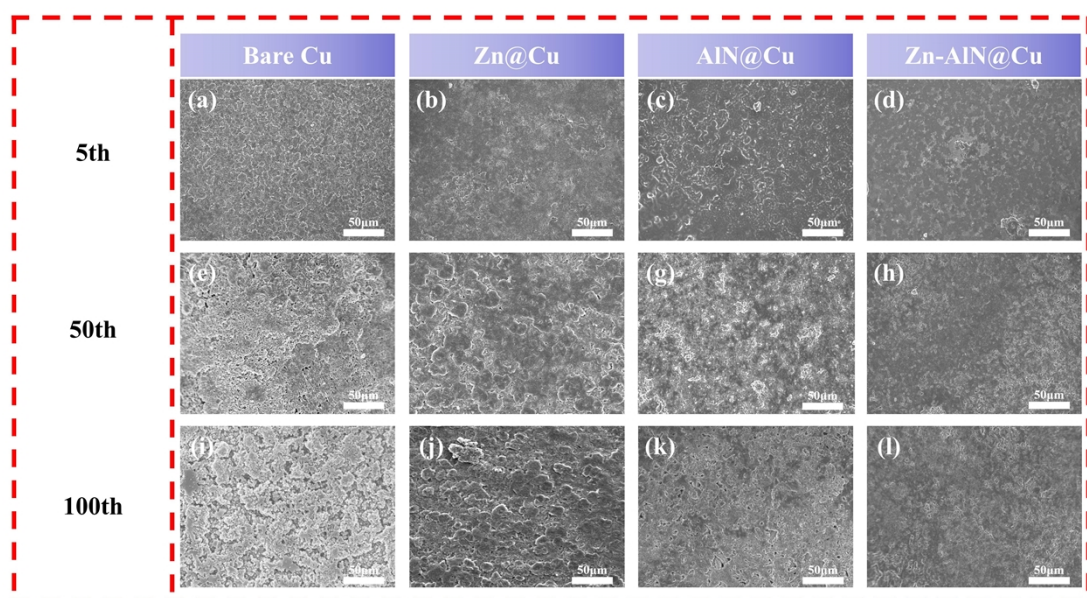

Figure S8. After lithium plating at 4mAh cm^{-2}, cross-sectional morphology of (a) Bare Cu, (b) Zn@Cu, (c) AlN@Cu, and (d) Zn-AlN@Cu.

**Li-Cu(100)**   **Li-Cu(110)**   **Li-Cu(111)**
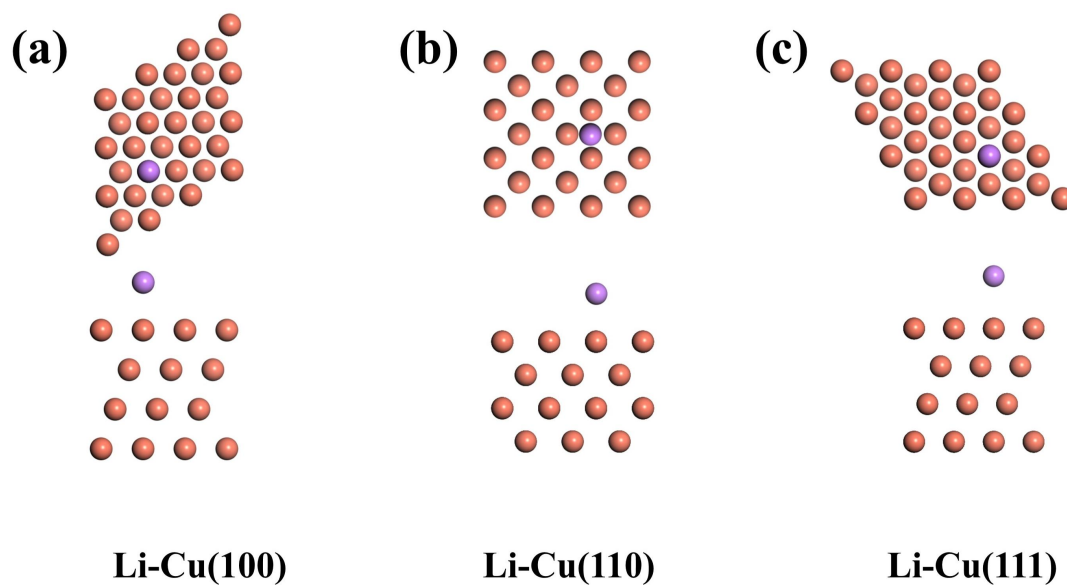
Figure S9. DFT calculations of Li adsorption on the different layers, Cu (100), Cu (110), and Cu (111).

Figure S10. Evolution of lithium deposition morphology with a fixed capacity of 1 mAh cm^{-2} and a fixed current density of 0.5 mA cm^{-2} on four CCs. (a), (c), and (i) are the surface morphology of bare Cu after 5, 50, and 100 cycles. (b), (f), and (j) are the surface morphology of Zn@Cu after 5, 50, and 100 cycles. (c), (g), and (k) are the surface morphology of AlN@Cu after 5, 50, and 100 cycles. (d), (h), and (l) are the surface morphology of Zn-AlN after 5, 50, and 100 cycles.
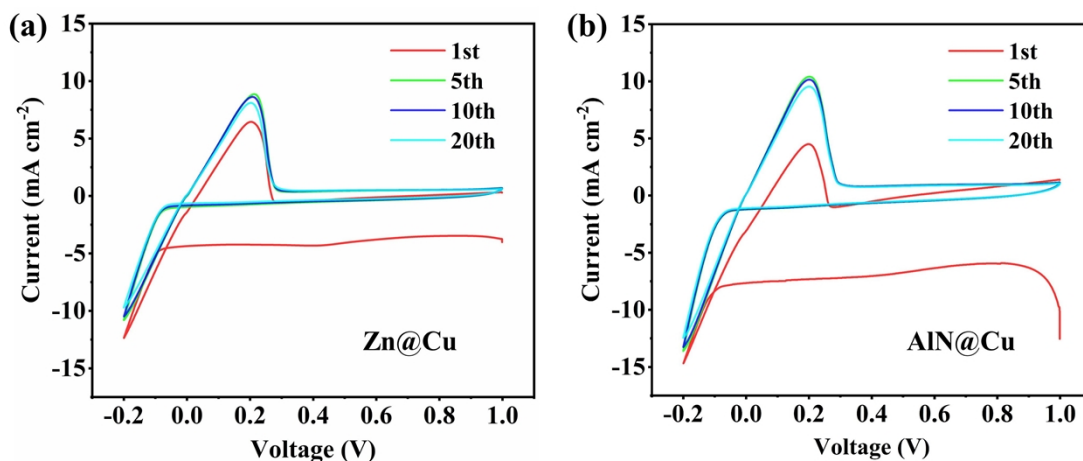
Figure S11. CV curves in the potential region of -0.2 to 1 V (vs Li$^+$/Li) at a scan rate of 0.5 mV s^{-1} of Li plating/stripping on (a) Zn@Cu, and (b) AlN@Cu electrodes.
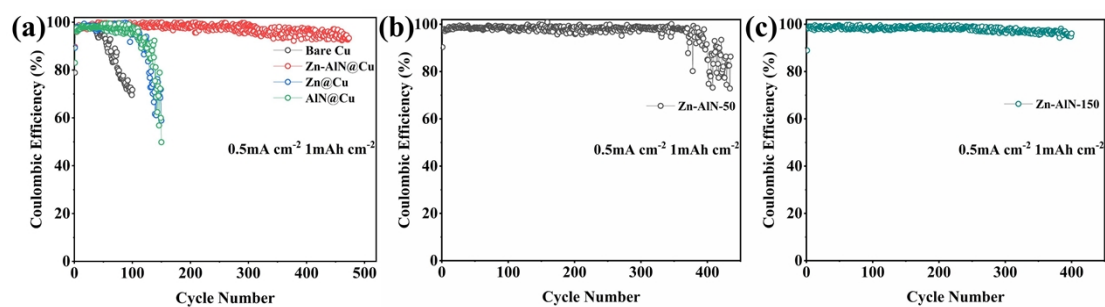
Figure S12. CE of Li plating/stripping on four CCs (a) at a current density of 0.5 mA cm^{-2} and a fixed areal capacity of 1 mAh cm^{-2} in a Lean electrolyte environment. CE of Li plating/stripping on (b) Zn-AlN-50 at a current density of 0.5 mA cm^{-2} and a fixed areal capacity of 1 mAh cm^{-2}, (c) Zn-AlN-150 at a current density of 0.5 mA cm^{-2} and a fixed areal capacity of 1 mAh cm^{-2}
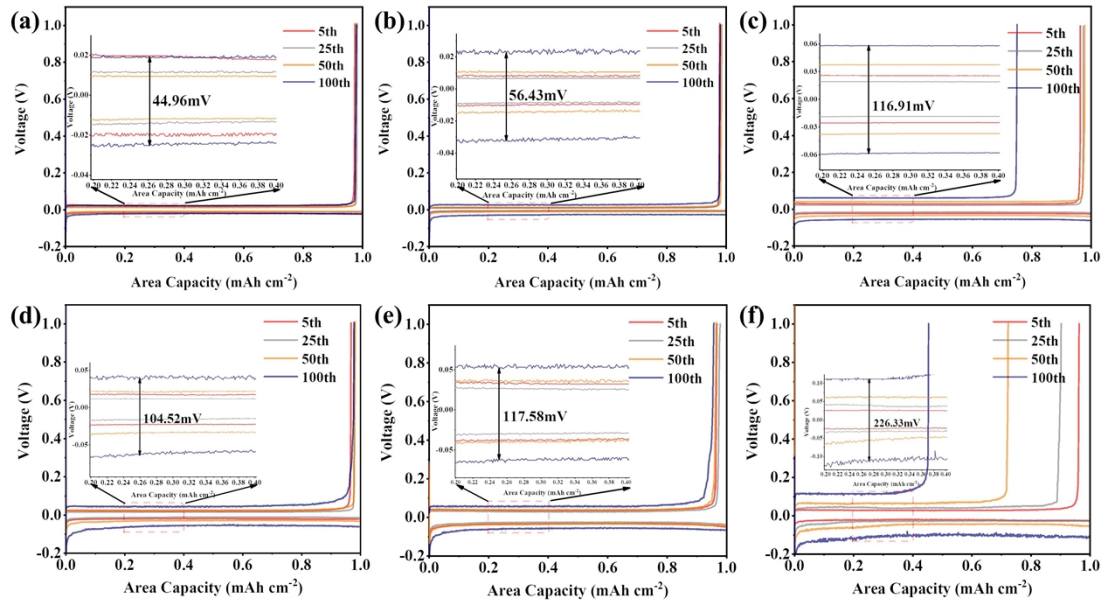
Figure S13. Voltage-area capacity profiles of AlN@Cu of Li plating/stripping under different cycles with (a) a fixed current density of 0.5 mA cm^{-2} and a fixed capacity of 1 mAh cm^{-2}, (d) a fixed current density of 2 mA cm^{-2} and a fixed capacity of 2 mAh cm^{-2}. Voltage-area capacity profiles of Zn@Cu of Li plating/stripping under different cycles with (b) a current density of 0.5 mA cm^{-2} and a fixed capacity of 1 mAh cm^{-2}, (e) a current density of 2 mA cm^{-2} and a fixed capacity of 2 mAh cm^{-2}. Voltage-area capacity profiles of bare Cu of Li plating/stripping under different cycles with (c) a current density of 0.5 mA cm^{-2} and a fixed capacity of 1 mAh cm^{-2}, (f) a current density of 2 mA cm^{-2} and a fixed capacity of 2 mAh cm^{-2}.
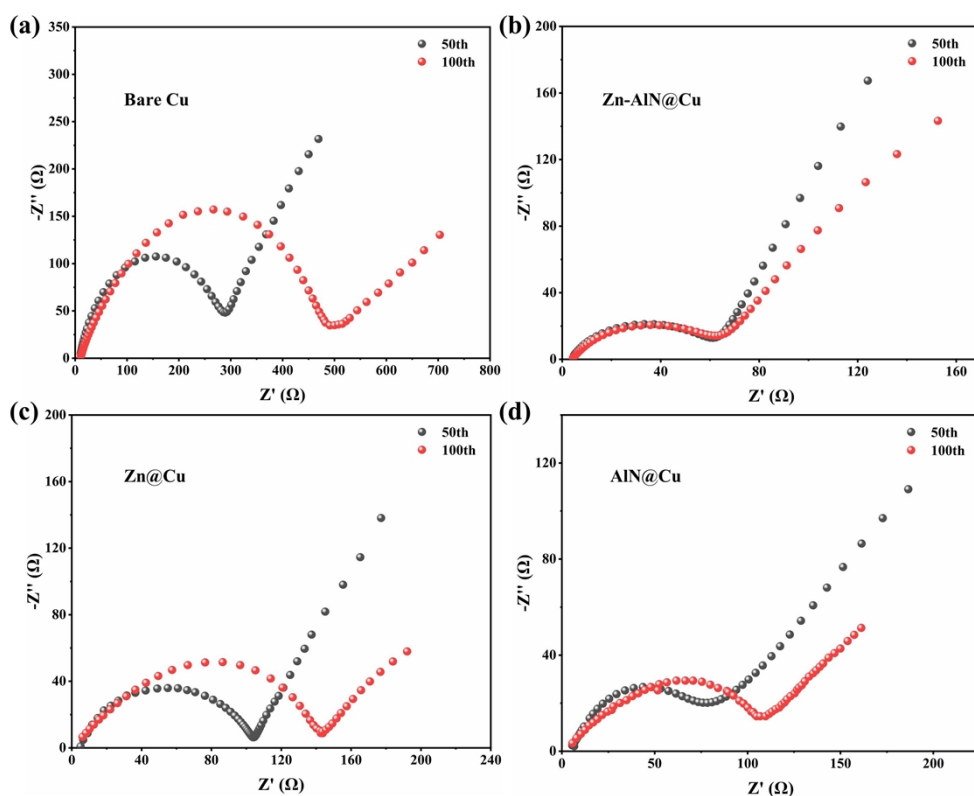
Figure S14. EIS curves of (a) bare Cu, (b) Zn-AlN@Cu, (c) Zn@Cu, and (d) AlN@Cu with 50th cycle and 100th cycle at a current density of 0.5 mA cm^{-2} and a fixed capacity of 1 mAh cm^{-2}

Table S1. Comparison of cycling performance of AFLMB using various strategies

Ref	Strategy	Electrolyte	Cathode Areal capacity (mAh cm^{-2})	Maximal Current (mA cm^{-2})	Capacity retention (%-cycle)
[S1][1]	GO@Cu	1 M LiTFSI in DOL/DME (1:1) + 1 wt% LiNO$_3$	NMC111, 1.77	0.2	44%-50
[S2][2]	PEO@Cu	1 M LiTFSI in DOL/DME (1:1) + 1 wt% LiNO$_3$	LFP, 0.765	0.153	30%-200

Ref	Material	Electrolyte	Cathode	Value	Retention-Cycles
[S3][3]	3D Electrode	1 M LiTFSI in DOL/DME (1:1) + 1 wt% LiNO$_3$	LFP,1.5	0.153	49.1%-100
[S4][4]	Cu$_3$N@Cu	1 M LiTFSI in DOL/DME (1:1) + 1 wt% LiNO$_3$	LFP,0.55	0.5	30%-50
[S5][5]	BTA@Cu	1 M LiTFSI in DOL/DME (1:1) + 1 wt% LiNO$_3$	LFP,1.5	0.75	73.3%-50
[S6][6]	3 M LiFSI in DOL/DME (1:1)		LFP,1.6	0.5	40%-100
[S7][7]	2 M LiFSI+1 M LiTFSI in DOL/DME (1:1)		LFP,1.6	0.2	32%-100
[S8][8]	1 M LiFSI in DME+ 1 M LiNO$_3$		LFP,1.7	0.2	66%-50
[S9][9]	rGO@Cu	1 M LiTFSI in DOL/DME (1:1) + 1 wt% LiNO$_3$	LFP,2.23	1.05	41%-100
[S10][10]	TEG@Cu	1 M LiTFSI in DOL/DME (8:2) + 3 wt% LiNO$_3$	LFP,16.9	1.36	71.3%-150
This work	Zn-AlN@Cu	1 M LiTFSI in DOL/DME (1:1) + 1 wt% LiNO$_3$	LFP,0.8	0.38	75.8%-50
					66.3%-100
			LFP,1.7	0.81	69.1%-50
					57.9%-100

Table S2 Comparison of the AFLMBs performance and commercial viability of various modification strategies

Ref	Strategy	Modification method	Cathode Areal capacity (mAh cm^{-2}) and rate	Capacity retention (%-cycle)	Modification efficiency and cost
[S11][11]	Sn@Cu	Vacuum Evaporation	LFP, 1.48, 0.1 C	57%-90	4.2 nm/min, total of 10 minutes, **Cheap**
[S12][12]	CuO@Cu	Thermostatic Heater	NCM523, 3, 0.5 C	41%-100	Total of 10 minutes, **Cheap**
[S13][13]	ULL@Cu	ALD	LCO, 2, 0.5 C	98.5%-50	6 nm/min, total of 10 minutes, **Expensive**
[S14][14]	NbO@Cu	ALD	NCM811, 0.5, 0.2 C	46%-100	15 nm/min, total of 10 minutes, **Expensive**
[S15][15]	Sn@Cu	Electroless Plating	NCM811, 4, 0.3 C	85.5%-100	Total of 2 minutes, **Rational**
[S16][16]	Ti$_3$C$_2$T$_x$@Cu	Spin-Coating	NCM811, 4.2, 0.2 C	70.9%-50	Total of 24 h, **Rational**
[S17][17]	CuO@Cu	Heat-Treated	LFP, 3.5, 0.2 C	37%-100	total of 15 minutes, **Cheap**
[S18][18]	Zn@NC@RGO@Cu	Metal Ion-dopamine Coordination	LFP, 1.6, 0.3 C	61.4%-100	Total of 26 h, **Expensive**
[S19][4]	Cu$_3$N@Cu	Magnetron Sputtering	LFP, 0.55, 1 C	30%-50	25 nm/min, total of 20 minutes, **Rational**
This work	Zn-AlN@Cu	Co-FCVA	LFP, 0.8, 0.5 C	66.3%-100	35-40 nm/min, total of 15 minutes, **Cheap**
			LFP, 1.7, 0.5 C	57.9%-100	35-40 nm/min, total of 15 minutes, **Cheap**

References

1 Z. T. Wondimkun, T. T. Beyene, M. A. Weret, N. A. Sahalie, C. Huang, B. Thirumalraj, B. A. Jote, D. Wang, W. Su, C. Wang, G. Brunklaus, M. Winter and B. Hwang, *J. Power Sources*, 2020, **450**, 227589.

2 A. A. Assegie, J. Cheng, L. Kuo, W. Su and B. Hwang, *Nanoscale*, 2018, **10**, 6125-6138.

3 H. Liu, X. Yue, X. Xing, Q. Yan, J. Huang, V. Petrova, H. Zhou and P. Liu, *Energy Storage Mater.*, 2019, **16**, 505-511.

4 Q. Li, H. Pan, W. Li, Y. Wang, J. Wang, J. Zheng, X. Yu, H. Li and L. Chen, *Acs Energy Lett.*, 2018, **3**, 2259-2266.

5 T. Kang, J. Zhao, F. Guo, L. Zheng, Y. Mao, C. Wang, Y. Zhao, J. Zhu, Y. Qiu, Y. Shen and L. Chen, *Acs Appl. Mater. Interfaces*, 2020, **12**, 8168-8175.

6 T. T. Beyene, B. A. Jote, Z. T. Wondimkun, B. W. Olbassa, C. Huang, B. Thirumalraj, C. Wang, W. Su, H. Dai and B. Hwang, *Acs Appl. Mater. Interfaces*, 2019, **11**, 31962-31971.

7 T. T. Beyene, H. K. Bezabh, M. A. Weret, T. M. Hagos, C. Huang, C. Wang, W. Su, H. Dai and B. Hwang, *J. Electrochem. Soc.*, 2019, **166**, A1501.

8 R. Rodriguez, R. A. Edison, R. M. Stephens, H. Sun, A. Heller and C. B. Mullins, *J. Mater. Chem. A*, 2020, **8**, 3999-4006.

9 Z. Hou, X. Wang, N. Zhan, Z. Guo, Q. Chen, J. Zhang, T. Bian, B. Hu and Y. Zhao, *Energy Storage Mater.*, 2022, **53**, 254-263.

10 Y. Wang, Z. Qu, S. Geng, M. Liao, L. Ye, Z. Shadike, X. Zhao, S. Wang, Q. Xu, B. Yuan, X. Zhang, X. Gao, X. Jiang, H. Peng and H. Sun, *Angew. Chem. Int. Ed.*, 2023, **62**, e202304978.

11 Y. Li, M. Bu, C. Mu and C. Yang, *Mater. Lett.*, 2024, **355**, 135449.

12 H. Xia, Y. Wang and Z. Fu, *Appl. Surf. Sci.*, 2023, **617**, 156529.

13 J. Kim, G. R. Lee, R. B. K. Chung, P. J. Kim and J. Choi, *Energy Storage Mater.*, 2023, **61**, 102899.

14 K. Doyle-Davis, K. Adair, C. Wang, F. Zhao, S. Deng and X. Sun, *Battery Energy*, 2024, **3**, 20230051.

15 Z. Zhang, H. Luo, Z. Liu, S. Wang, X. Zhou and Z. Liu, *J. Mater. Chem. A*, 2022, **10**, 9670-9679.

16 X. Zeng, M. Mahato, W. Oh, H. Yoo, V. H. Nguyen, S. Oh, G. Valurouthu, S. Jeong, C. W. Ahn, Y. Gogotsi and I. Oh, *Energy Environ. Mater.*, 2024, **7**, e12686.

17 J. Chen, L. Dai, P. Hu and Z. Li, *Molecules*, 2023, **28**.

18 S. Huang, S. Lu, Y. Lv, N. Li, Z. Wu, G. Zhong, X. Ren, Y. Wang, B. Sun, Y. Huang, F. Kang and
Y. Cao, *Nano Res.*, 2023, **16**, 11473-11485.